



# Low Temperature Plasma Technology Laboratory

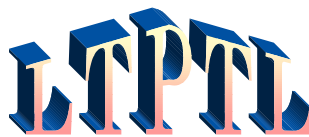
---

**Physical Mechanisms in  
Industrial RF Plasma Sources**

Francis F. Chen  
*Electrical Engineering Department*

LTP-104

April, 2001



Electrical Engineering Department  
Los Angeles, California 90095-1594

# Physical Mechanisms in Industrial RF Plasma Sources

Francis F. Chen

Electrical Engineering Department, University of California, Los Angeles  
Los Angeles, California, 90095-1594

**Abstract.** RF plasma sources are essential for producing semiconductor chips, but they are developed empirically, with incomplete knowledge of how they work. Inductively coupled plasmas (ICPs) employ rf fields without a dc magnetic field  $B_0$  and produce ionization well outside the skin layer. Helicon sources with a  $B_0$  can generate much higher densities but pose a number of puzzling physical questions. Of these, a selected few are discussed in this paper.

## ENERGY DEPOSITION IN INDUCTIVELY COUPLED PLASMAS

Figure 1 shows two common types of ICP, (a) with a spiral “stove-top” antenna, and (b) with an antenna wound on the cylindrical surface; others combine them with a dome-shaped coil. All can produce uniform plasmas, but type (b) does so even if the

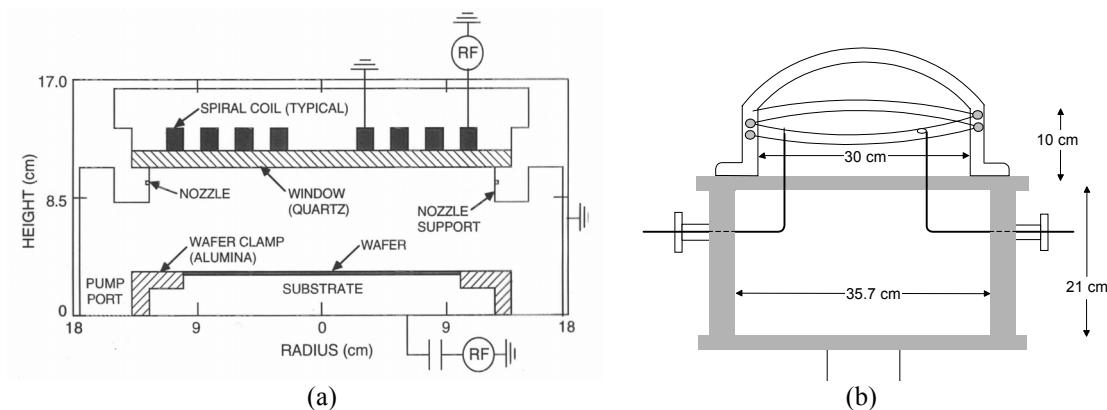


**FIGURE 1.** (a) A stove-top ICP (or TCP) and (b) an ICP with a loop or coil antenna.

skin depth  $d_s$  is  $\ll$  the discharge radius  $a$ . Typical plasma profiles taken in device (b) are shown in Fig. 2a, and the B-dot signal on a log scale in Fig. 2b. Note that the density  $n$  is peaked instead of hollow, even though the skin depth is only about 3 cm. When the rf field has fallen to  $\approx 1\%$  of its maximum, it sometimes rises again (Fig. 2b) with a null at which the phase jumps by  $180^\circ$ . Neither of these effects is predictable from linear theory, and they have been attributed to the *anomalous skin effect*<sup>1</sup>, in which thermal motions carry inward those electrons accelerated in the skin

<sup>1</sup> V.I. Kolobov and D.J. Economou, Plasma Sources Sci. Technol. **6**, R1 (1997).

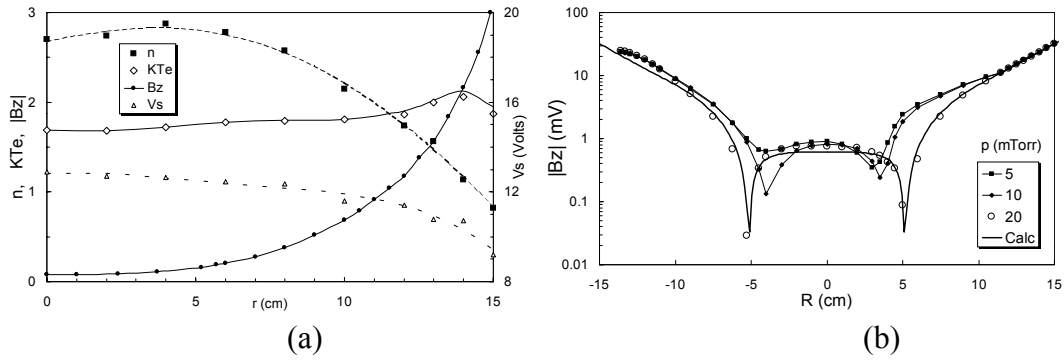
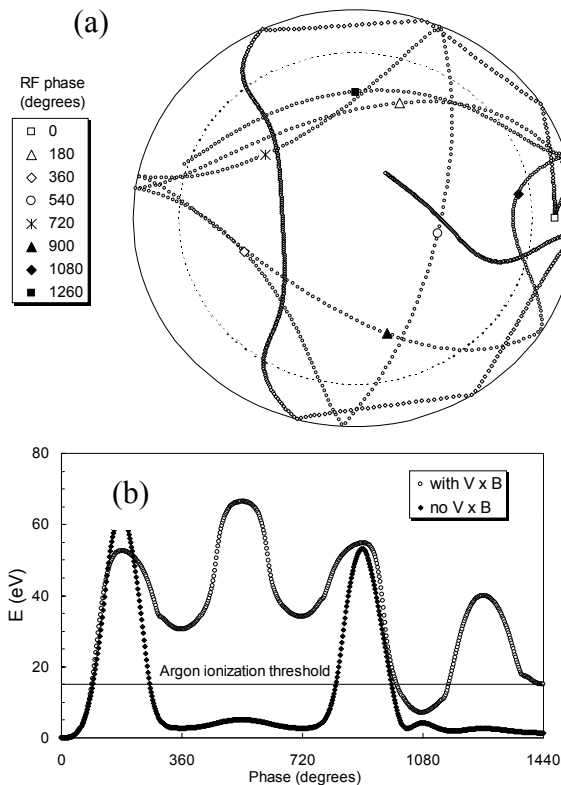


**FIGURE 2.** (a) Profiles of  $n$  ( $10^{11} \text{ cm}^{-3}$ ),  $KT_e$  (eV),  $V_s$  (V), and  $B_z$  (arbitrary units) in an ICP discharge in 10 mTorr of argon, with  $P_{\text{rf}} = 300\text{W}$  at 2 MHz. (b) Normalized semilog plot of  $|B_z|$  ( $r$ ) in the plane of the  $m = 0$  antenna at various pressures. The linear region corresponds to a skin depth of 3 cm. The 5- and 10-mTorr data are connected by lines, but the curve for the 20-mTorr data is a theoretical fit (see text). Conditions: 400W at 2 MHz, 5-20 mTorr of Ar.

layer (“skin”), or to the nonlinear generation of 2nd harmonics currents<sup>2</sup>. We believe the anomalies arise from separate causes. The presence of ionizing electrons in the interior can be seen by following the orbit of a single electron starting at an arbitrary position with an arbitrary velocity in the thermal range, and at an arbitrary phase of the rf field, as shown in Fig. 3a. In this example, the electron starts at rest inside the skin at the rf maximum and is accelerated in the  $\theta$  direction to help shield out the antenna’s



field. After  $180^\circ$ , it is driven in the  $-\theta$  direction. When it reaches a wall, it is made to bounce specularly. The two paths differ by inclusion of the Lorentz force  $\mathbf{F}_L = -e\mathbf{v} \times \mathbf{B}_{\text{rf}}$ . This radial force has the effect of pushing the electron inwards, or outwards to make a steeper angle with the wall. The energy  $W$  of the electron during the first four cycles is shown in Fig. 3b.

**FIGURE 3.** (a) Path of an electron starting at rest ( $\square$ ) with (marked path) and without (unmarked path) inclusion of the  $\mathbf{v} \times \mathbf{B}$  force  $\mathbf{F}_L$ . The triangles ( $\Delta$ ) mark the positions where  $E_\theta$  changes sign. The points are 1 nsec apart. The outer circle is the sheath boundary at  $r = a$ , and the inner circle is smaller by a skin depth of 3.1 cm.  $E_\theta(a) = -8 \text{ V/cm}$ ;  $B_z(a) = -7 \text{ G}$ . (b) Energy of the electrons following the orbits in (a). The upper curve includes  $\mathbf{F}_{\text{NL}}$ ; the lower does not.

It is seen that, without  $\mathbf{F}_L$ ,  $W$

<sup>2</sup> V.A. Godyak, R.B. Piejak, and B.M. Alexandrovich, Phys. Rev. Lett. **83**, 1610 (1999).

exceeds 15 eV only when the electron is in the skin; with  $\mathbf{F}_L$ , it carries large energy into the interior. Though each orbit is different, electrons accelerated while in the skin can, on average, reach the interior by (a) the  $\mathbf{F}_L$  force, (b) sharp reflections from the curved wall, and (c) fortunate phasing relative to the rf field.

In the following 2D Monte Carlo calculation, elastic and inelastic collisions with neutrals are taken into account. A sheath of negligible thickness is assumed on the cylindrical wall, forming a Coulomb barrier of specified magnitude  $V_{sh}$  ( $\approx 20$  eV). If an electron reaches the sheath with perpendicular energy  $< V_{sh}$ , it is reflected specularly; otherwise, it is lost to the wall. Lost electrons are replaced by new ones born at an arbitrary position in the cross section with an arbitrary velocity corresponding to a Maxwellian distribution at a specified temperature  $KT_e$ . The rf field of specified strength has a profile computed from classical theory for an infinite cylinder with uniform  $n$ ,  $KT_e$ , and pressure  $p$ . The first part of a typical 80- $\mu$ s run is shown in Fig. 4. Discontinuities in the orbit due to collisions and wall reflections can be seen.

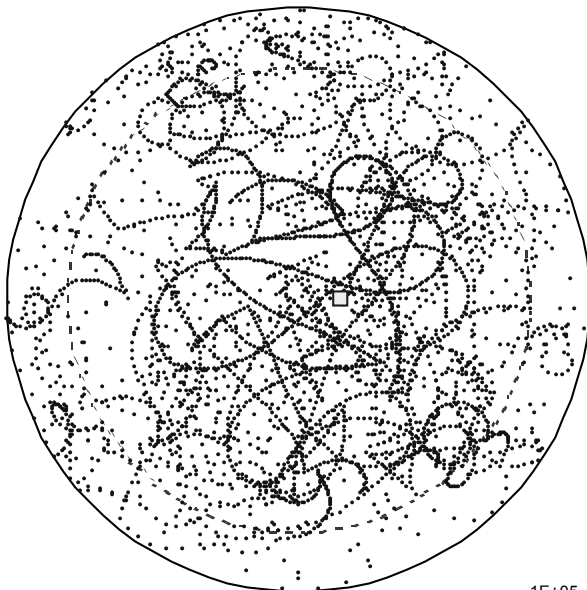
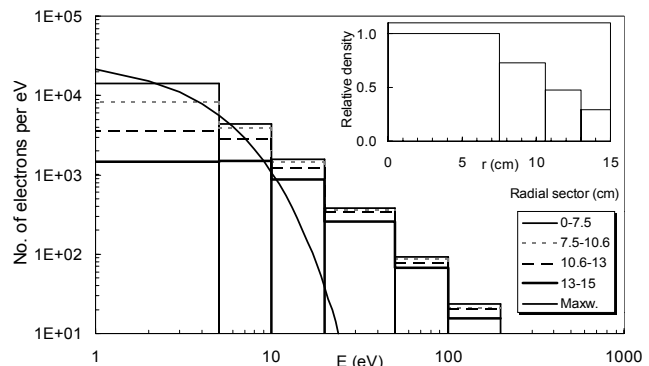


**FIGURE 4.** An electron orbit in 2.5-nsec steps. Conditions:  $n = 3 \times 10^{10} \text{ cm}^{-3}$ ,  $KT_e = 3 \text{ eV}$ ,  $p = 10 \text{ mTorr Ar}$ ,  $a = 15 \text{ cm}$ ,  $f = 2 \text{ MHz}$ ,  $V_{sh} = 20 \text{ V}$ ,  $E_{\theta}(a) = -5 \text{ V/cm}$

In this run, there were 3746 elastic and 3 inelastic collisions, the electron was lost to the wall 178 times, and its average energy was 21.2 eV. The distribution  $f_e(v)$  compiled at different radii is shown in Fig. 5, together with the density  $n(r)$ .

**FIGURE 5.** Monte Carlo calculation of  $f_e(v)$  in four radial regions of equal area. The inset shows the density profile. The curved line is a 3-eV Maxwellian distribution (log-log scale).

It is seen that an appreciable non-Maxwellian tail of ionizing electrons exists at all radii. The density peak on axis, often seen experimentally, is caused by slow electrons born outside the skin which remain in the interior for many rf cycles before they wander out to the high-field region.



The effect of Fig. 2b is too small to affect the discharge equilibrium but is a curious phenomenon, since no “standing waves” of this type are predicted by classical electromagnetics. We believe that it is caused by a current ring which breaks away from the usual skin current because it is preferentially pushed inwards by  $\mathbf{F}_L$  at the  $E$ -field

maximum. This current-carrying structure (CCS) looks like a diffuse  $\theta$ -pinch (Fig. 6), has its own  $L/R$  decay time, and drifts inwards as  $E$  decays, maintaining magnetic pressure balance. When  $L/R$  is  $\geq$  a half rf period, the CCS current maintains its direction while a reversed skin current grows in the next half cycle, thus causing the null in  $B_z$  at an intermediate radius. The theoretical curve in Fig. 2b fits the 20 mTorr data rather well. Details on the CCS picture, as well as on the orbit calculations, have been given by John Evans<sup>3</sup>.

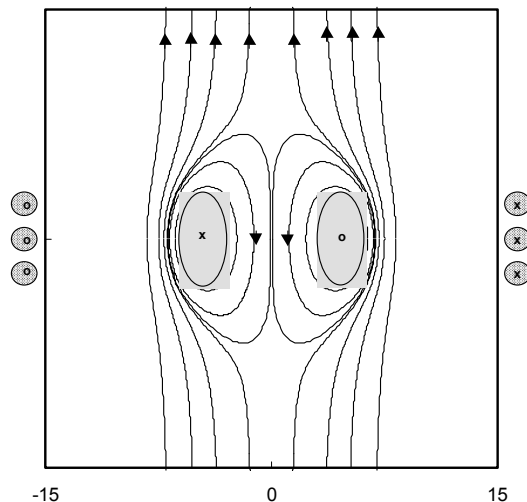


**FIGURE 6.** Magnetic field lines around an elliptical, bi-Gaussian CCS with  $R = 4.5$ ,  $b = 1.5$ , and  $c = 3$  cm, imbedded in the time-averaged skin field of an  $n = 8 \times 10^{10} \text{ cm}^{-3}$  plasma with  $p = 10$  mTorr,  $KT_e = 3$  eV, and  $f = 2$  MHz. The box is  $15 \times 15$  cm, and the curvature of the skin field is neglected.

## PHYSICS OF HELICON DISCHARGES

Helicon discharges are based on launching whistler waves confined to a cylinder, and the coupling to the rf system is so efficient that  $\approx 10^{14} \text{ cm}^{-3}$  densities can be attained with only 2-3 kW of power. Commercial units have lower  $n$  and are designed to cover large areas uniformly. Basic studies of helicons, however, are usually done in 2-4 cm diam tubes in long, uniform fields  $B_0$ , such as that shown in Fig. 7. Helicon

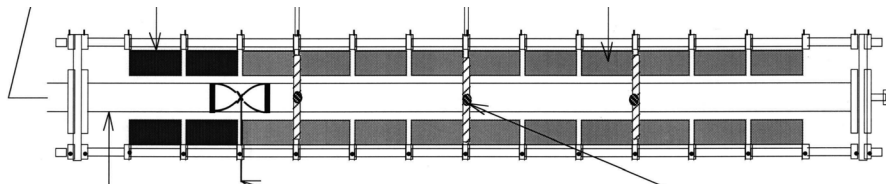


**FIGURE 7.** Research helicon device, 160 cm long.

waves propagate with an axial wavenumber  $k$  along  $\mathbf{B}_0$  and rotate with azimuthal mode number  $m$  in the clockwise (RH,  $m > 0$ ) or counterclockwise (LH,  $m < 0$ ) direction, viewed along  $\mathbf{B}_0$ . Helical antennas matching the wave shape are found to be the most efficient. A full wavelength,  $m = 1$  antenna is shown in Fig. 8;  $m = 0$  is also used.

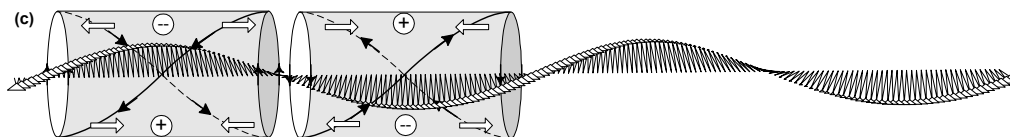


**FIGURE 8.** An  $m = +1$  wave launched to the right by a helical antenna; in principle, an  $m = -1$  wave should be launched to the left simultaneously.

The first question is: Why are helicon discharges so much more efficient than other rf sources? The typical 0.1-1 kG  $\mathbf{B}_0$  fields increase the skin depth and confine the

<sup>3</sup> J.D. Evans and F.F. Chen, Phys. Rev. Letters **86**, 0000 (2001).

electrons radially, to be sure, but these are minor effects. We originally suggested that energy is absorbed by Landau damping, since the phase velocity of helicons can be made to match the optimum velocity of ionizing electrons. Although many authors claimed to have verified this, our own work, using a time-resolved gridded energy analyzer<sup>4</sup>, failed to find a significant number of non-Maxwellian electrons. Indeed, these are not necessary: a 3-eV Maxwellian already provides too much ionization, and neutral pumpout has to be assumed to achieve discharge equilibrium at high powers. Since collisional damping of helicon waves is weak, how does the rf energy get transferred to the electrons? The answer came from including the finite electron mass, which is normally neglected since  $\omega \ll \omega_c$ . This yields a second root to the dispersion relation, as shown in Fig. 9. The new wave, of short radial wavelength, is an electron cyclotron wave, known as a Trivelpiece-Gould (TG) mode in cylindrical geo-

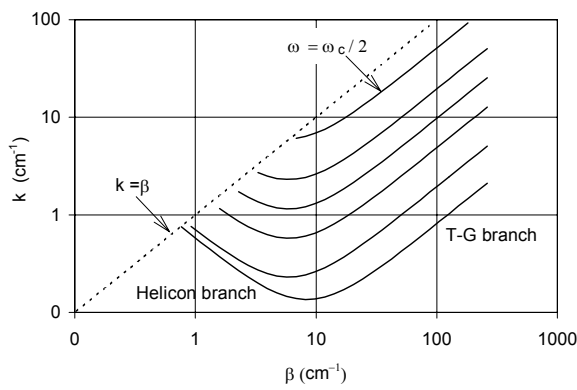


**FIGURE. 9** Parallel vs radial wavenumber for various  $B_0$ , increasing downwards. For each  $k$ , two values of  $\beta$  are excited; the TG branch has short radial wavelength.

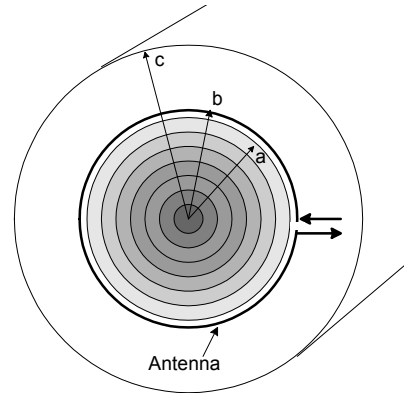


**FIGURE 10.** Geometry of the ANTENA code.

metry. The helicon (H) wave is excited by the antenna, which is designed to match its wavelength. At the boundary  $r = a$ , the TG mode is generated to satisfy the boundary condition. Being electrostatic, the TG wave is rapidly absorbed as it propagates inwards. Thus, the absorption efficiency is due to mode conversion to the strongly damped TG wave. At high  $B_0$ , this wave is localized close to  $r = a$ ; to treat it properly requires using a realistic density profile. The ANTENA code used in rf heating does this by dividing the plasma into many uniform shells and matching across each boundary (Fig. 10). We have improved on this by expressing the density-gradient ( $\nabla n$ ) terms analytically<sup>5</sup>. Using these expressions, D. Arnush has developed a code HELIC<sup>6,7</sup>, which runs rapidly on a PC. When results are compared with the ANTENA code, we find that they differ: the ANTENA code is in error because the  $\nabla n$  terms had not been included in the jump conditions at the shell boundaries. Figure 11a shows that the radial absorption profile is quite different if these terms are included; Fig. 11b shows the importance of including the TG mode; and Fig. 12 shows that the density profile makes a considerable difference.

<sup>4</sup> F.F. Chen and D.D. Blackwell, Phys. Rev. Lett. **82**, 2677 (1999).

<sup>5</sup> F.F. Chen, M.J. Hsieh, and M. Light, Plasma Sources Sci. Technol. **3**, 49 (1994).

<sup>6</sup> D. Arnush and F.F. Chen, Phys. Plasmas **5**, 1239 (1998).

<sup>7</sup> D. Arnush, Phys. Plasmas **7**, 3042 (2000)

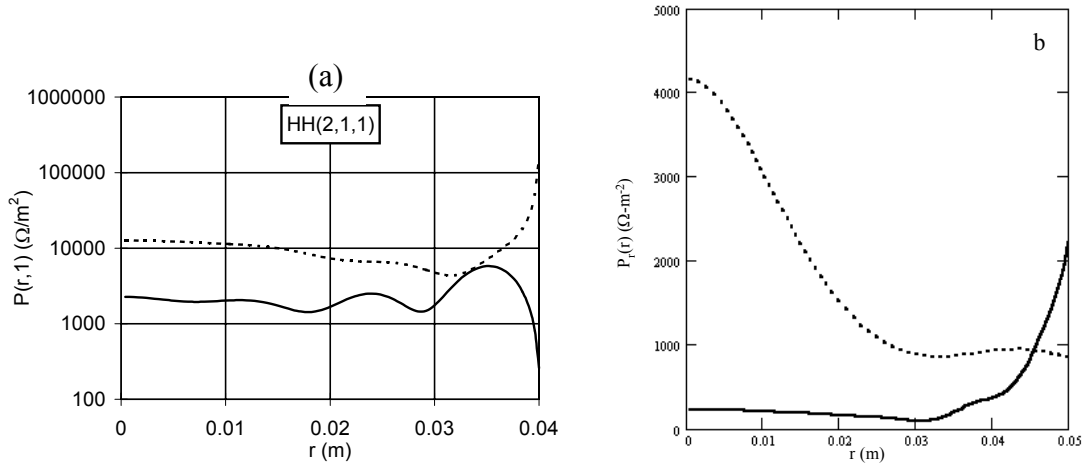


**FIGURE 11.** Radial power deposition profiles  $P(r)$  from the HELIC code: (a) with (—) and without (---) the  $\nabla n$  terms for a parabolic  $n(r)$ ; (b) with (—) and without (----) the TG mode for uniform  $n(r)$ .

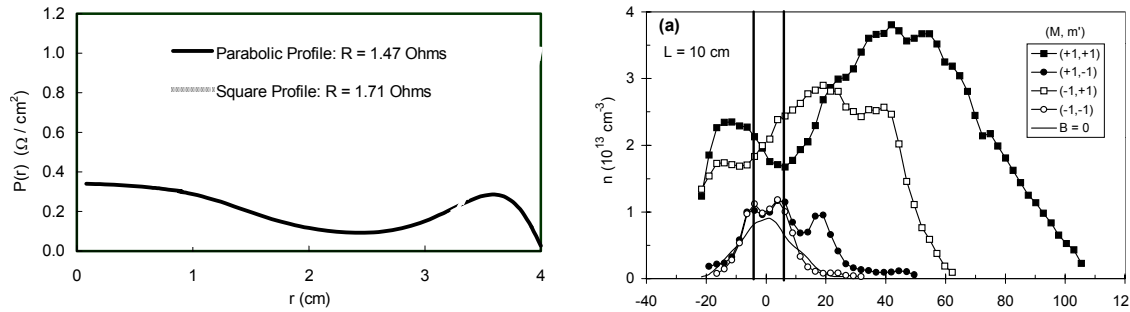


**FIGURE 12.** Typical  $P(r)$  profiles for a parabolic  $n(r)$  (—) and for a uniform plasma. Also shown is the total loading resistance, which agrees well with measurements.

**FIGURE 13.** Axial density profiles  $n(z)$  with a bifilar antenna located as shown at  $z = 0$  cm. The top two curves have the rf field rotating in the  $m = +1$  direction. The bottom curve is for an ICP with no dc magnetic field.

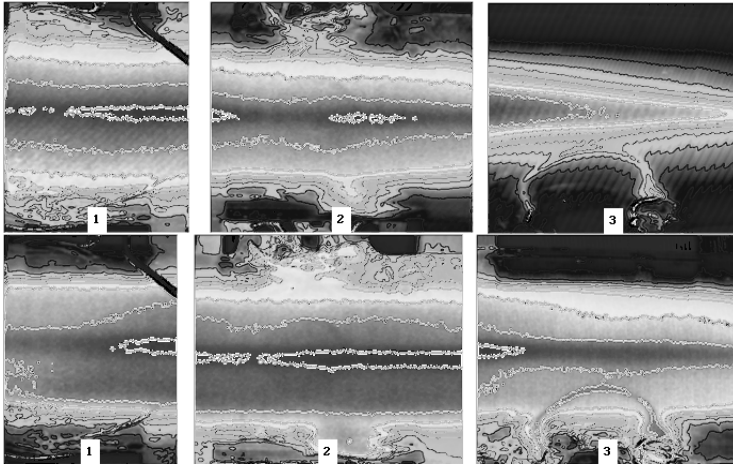
D. Miljak<sup>8</sup> used a bifilar helical antenna with variable phase to produce rf fields rotating in the  $m = +1$  or  $-1$  directions in time. The helix can also match  $m = 1$  or  $-1$  in space. The highest density seen in Fig. 13 is found when the  $m = 1$  mode is excited both in time and in space. The second curve is for  $m = +1$  in time and  $m = -1$  in space. The low curves are for  $m = -1$  in time and  $m = \pm 1$  in space. Thus, the  $m = +1$  (RH polarized) mode is dominant, and it is more efficiently excited by rotation in time than rotation in space.

That the RH mode propagates better has also been seen directly by Blackwell<sup>9</sup>, whose photographs of  $\text{Ar}^+$  emission at three axial positions are shown in Fig. 14. Furthermore, measurements of  $\mathbf{B}(r)$  by Light<sup>10</sup> (Fig. 15) show agreement with the theoretical  $m = +1$  profiles even when the antenna helicity was set for the  $m = -1$  mode. Although whistler waves in free space have RH polarization, it is surprising

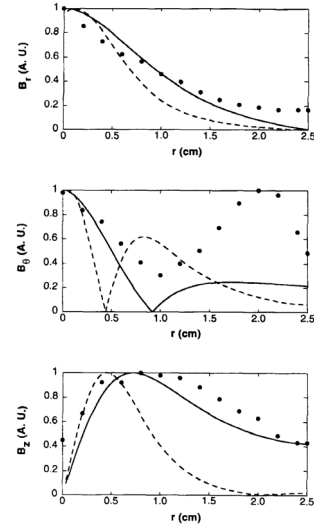
<sup>8</sup> D.G. Miljak and F.F. Chen, Plasma Sources Sci. Technol. **7**, 61 (1998).

<sup>9</sup> D.D. Blackwell and F.F. Chen, Plasma Sources Sci. Technol. **6**, 569 (1997).

<sup>10</sup> M. Light and F.F. Chen, Phys. Plasmas **2**, 1084 (1995).



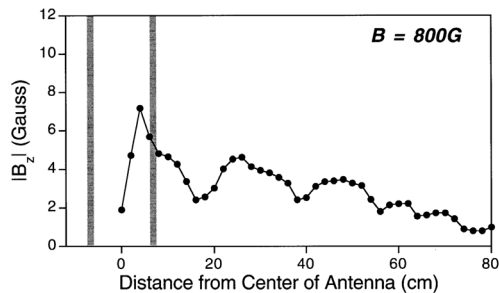
**FIGURE 14.** Sideviews of an  $m = -1$  (top) and  $m = +1$  (bottom) helicon discharges at ports 30 cm apart. The antenna is in the left-hand frame.



**FIGURE 15.** Radial profiles of  $B_r$ ,  $B_\theta$ , and  $B_z$  compared with theoretical curves for  $m = +1$  (—) and  $m = -1$  (---).

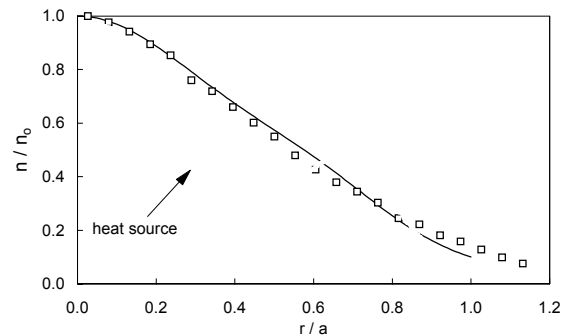
that the LH mode should be difficult to excite, since simple theory shows that both modes are identical in a cylinder except for a small difference in mode pattern. The explanation was provided by HELIC calculations. Apparently, the coupling to the  $m = -1$  mode is weak because of its narrower profile, which overlaps less with the TG mode at the boundary.

Figure 13 shows another puzzle: the maximum density occurs well downstream of the antenna region where the rf fields are strongest. We believe this arises because  $KT_e$  falls as  $z$  increases, due to radiative collisions, and electron pressure balance then causes the density to pile up. At large  $z$ , the plasma is lost to the wall. There is also some downstream ionization, but HELIC shows that this is weak at  $z = 50$  cm.



**FIGURE 16.** Non-monotonic decay of  $|B_z|$  away from the antenna located between the vertical bars.

Another mystery is shown in Fig. 16, where  $|B_z|$  is seen to undergo oscillations as the helicon wave travels away from the antenna. This beating phenomenon is caused by simultaneous launching of two radial modes with slightly different  $k$ . The computed  $k$ -spectrum excited by the helical antenna correctly predicts the wavelength of the beats.

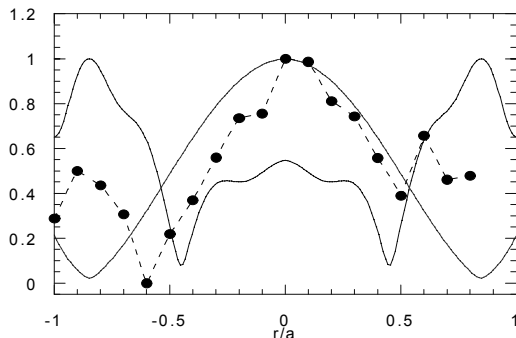


**FIGURE 17.** A “triangular”  $n$  profile and a theoretical curve (—) computed for a bimodal source distribution.

At densities  $>10^{13} \text{ cm}^{-3}$ , the  $n(r)$  profile often has a surprising shape, more triangular than parabolic (Fig. 17). Such a shape is not consistent with ordinary neutral diffusion for any reasonable ionization function. At high densities, however, neutrals are depleted by ion pumping, and ion-electron collisions dominate. Since Ar ions are unmagnetized for  $B_0 < 1\text{kG}$  and electrons can diffuse readily via the Simon short-circuit effect, radial diffusion is controlled by  $D_i \propto 1/v_{ei} \propto 1/n$ . This nonlinear diffusion coefficient coupled with a double-peaked ionization profile (*cf.* Fig. 12), can give “triangular”  $n$  profiles agreeing with measurements (Fig. 17).

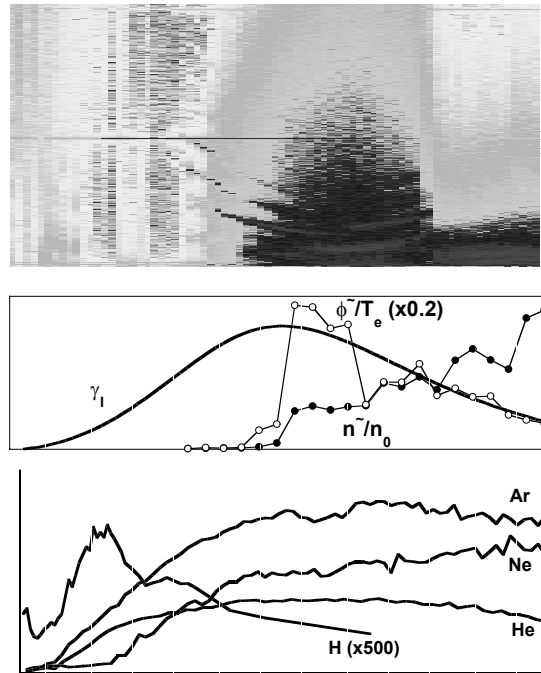
Although the helicon dispersion relation predicts  $n \propto B_0$ , at high fields  $n$  begins to saturate in Ar, and in light gases actually reaches a peak and falls with  $B_0$ . In his Ph.D. thesis, M. Light found a low-frequency instability that grows just as  $n$  begins to saturate (Fig. 18). The theoretical growth rate  $\gamma_1$  peaks just at this  $B_0$ , and  $\langle n - \phi \rangle$  correlations show an enhanced radial flux. However, the physics is not simple: this calculated flux stops short of the edge. The loss is by axial flow, and the fluctuations serve to bring plasma to larger radii, where there is a larger area for endloss.

**FIGURE 18.** (a) Neon frequency spectrum (0 – 20 kHz) vs  $B_0$ , (0 to 1.5kG); (b) calculated growth rate and measured  $n$  and  $\phi$  oscillation amplitudes; (c)  $n_0$  vs  $B_0$  in various gases.



**FIGURE 19.** RF current  $j(r)$  compared with theory with and without the TG mode.

This paper has embraced the work of numerous colleagues and students, often without reference for lack of space: Don Arnush, Dave Blackwell, John Evans, Max Light, Tsitsi Madziwa, David Miljak, Kostia Shamrai, and Kiko Sudit. It has been a pleasure to work with them.



Since the TG mode is essential to understanding the ionization mechanism in helicon discharges, we have attempted to detect it directly. This can be done only at low fields, around 30G, where the mode has a large enough radial wavelength to be seen. To do this, Blackwell and Madziwa built an rf Rogowski coil to detect the current profile  $j(r)$ , which is much more sensitive to the TG mode than  $B_z(r)$ . In Fig. 19, the points show the side peaks of the TG mode